A Cyclone/Anticyclone Couplet over North America: An Example of Anticyclone Evolution

JAMES S. BOYLE[1] AND LANCE F. BOSART

Department of Atmospheric Science, State University of New York at Albany, Albany, NY 12222

(Manuscript received 2 June 1982, in final form 8 February 1983)

ABSTRACT

A detailed case study has been made of a cyclone/anticyclone couplet over North America during early winter, 11–18 November 1969. The anticyclone was the dominant member of the couplet in this case.

Objective analyses of the wind and mass fields were carried out in both the isobaric and isentropic coordinate systems. Calculated quantities which are discussed include quasi-geostrophic vertical velocity and height tendency, potential vorticity, and quasi-Lagrangian kinetic energy budgets.

The movement of the cold, polar anticyclone out of its source region in Alaska southeastward to the Gulf of Mexico is seen to be thermally steered. During this stage the anticyclone moves toward the region of descent forced by the low level cold advection. As the anticyclone recurves and begins to move northeastward along the east coast of the United States, it becomes a warm, dynamic system. The forcing directing the movement is that of differential vorticity advection. The static stability structure of the anticyclone changes in a manner consistent with this changeover in forcing in that the lower troposphere becomes more stable and the upper troposphere becomes somewhat less stable. Calculations show that the strong cyclogenetic diabatic forcing created by cold air flowing over warm water along the east coast is overwhelmed by the quasi-geostrophically driven height rises.

The mechanism by which the cold air dome associated with the anticyclone moves southward intact is explained from two complementary perspectives. One viewpoint is that of asymmetries in the jet stream about the long wave trough with a jet streak to the west of the cold dome. The other is that a maximum in potential vorticity located above the coldest air will prevent the dome from subsiding. The migration of the jet streak to the eastern side of the cold dome and the movement of the potential vorticity maximum from its position over the cold air lead to collapse of the cold air and induce cyclogenesis on the eastern side of the cold air. Furthermore, the calculations show that the potential vorticity is not at all conserved in the region of the deepening cyclone.

The kinetic energy budgets indicate that the anticyclone region serves as a source of upper level energy for the downstream cyclone. The collapse of the cold air converts potential to kinetic energy and this energy is fed into the jet streak on the eastern side of the long wave trough.

1. Introduction

Reiter (1969) estimates that the amount of literature pertaining to anticyclones is an order of magnitude less than that concerning cyclones. In this work, an attempt is made to consider both anticyclonic and cyclonic components of an evolving anticyclone/cyclone couplet. In the case considered here the anticyclone is the dominant member of the couplet.

The basic approach is that of a traditional case study as outlined by Pearce (1974). The theoretical framework upon which the study is grounded is that of quasi-geostrophic (QG) theory. Detailed analyses of the mass and wind fields were carried out on both isobaric and isentropic (constant virtual potential temperature) surfaces.

The outline for the paper is as follows. Section 2 contains a description of the data handling and objective analysis procedures. Section 3 provides an extensive synoptic description of the case considered. Section 4 describes the QG calculations of vertical motion and height tendency and contains a discussion of the result of the computations. Also in this section is a QG diagnosis of the effect of sensible heat transfer on the progress of the anticyclone off the eastern United States. In Section 5 the computed fields of potential vorticity on isentropic surfaces are related to events in the evolution of the cyclone/anticyclone couplet. Section 6 contains a description of the quasi-Lagrangian kinetic energy budget of the couplet. Budgets are computed for both the cyclone and anticyclone regions and the properties of each are compared. Section 7 provides a brief summary and chief conclusions drawn from the preceding results.

[1] Present Affiliation: NRC Research Associate, Department of Meteorology, Naval Postgraduate School, Monterey, CA 93940.

2. Data handling and analysis procedures

The basic meteorological observations were obtained from a number of sources. Surface observations were taken from tapes produced by the Air Force Environmental Technical Applications Center and supplied by the National Climatic Center. Upper air sounding data were selected from the National Meteorological Center's (NMC) Automatic Data Processing tapes supplied by the National Center for Atmospheric Research (NCAR). Both of these basic data sets were supplemented by data obtained from teletype reports, the Canadian Meteorological Bulletin of Upper Air Reports, Northern Hemisphere Data Tabulations, dropsonde and reconnaissance aircraft reports. Essential to the success of the isentropic analyses was the ability to provide significant level data as well as mandatory level data for as many soundings as possible. This involved extensive augmentation of the tape data which often provided information at mandatory pressure levels only. The rawinsonde data were processed to provide values at 100 mb intervals for the pressure analyses and every 4 K for the isentropic analyses. The processing programs for this work followed the procedures of Bleck and Haagenson (1968).

The processed surface and upper air data were objectively analyzed onto a polar stereographic grid with a horizontal spacing of 190.5 km at 60°N. The grid orientation is identical to that of the NMC octagonal hemispheric grid with the y-axis coincident with 80°W. The grid size was 37 by 33 points. The vertical spacing for the pressure surface analyses was 100 mb, the levels extending from 1000 mb to 100 mb. The vertical increment for the isentropic analysis was 4 K from 244 K to 340 K and 8 K from 340 K to 380 K. Thus the pressure analyses had 10 levels and the isentropic analyses had 30 levels.

The objective analysis technique used was that of optimum interpolation as modified by Bleck (1975). The analyses were all univariate with geostrophic correlations used for the wind component analyses, Schlatter *et al.* (1976). The fields analyzed on pressure surfaces were height, temperature and the wind components. The fields analyzed on isentropic surfaces were the Montgomery streamfunction ($M \equiv C_pT + gZ$), pressure, stability ($\partial\theta/\partial p$) and the wind components. The first guess fields were derived from the NMC operational analysis and from rawinsonde and surface observations; more details are provided in Boyle (1981).

3. Synoptic description

The purpose of this section is to provide a synoptic overview of the case considered here. A graph of the central pressure of the anticyclone and cyclone versus time period for the couplet is presented in Fig. 1. Table 1 relates the time periods of the study to the appropriate date time group. Figures 2 and 3 present the 1000 mb heights, the 1000–500 mb thickness, the 300 mb heights and isotachs for period 3 and succeeding periods spaced 24 hours apart. The positions of the anticyclone and cyclone at each time period are indicated on Fig. 2. The anticyclone–cyclone couplet is not formed until periods 7 and 8, when cyclogenesis takes place near the Chesapeake Bay region. As seen in Fig. 1 by period 3 the anticyclone is at its

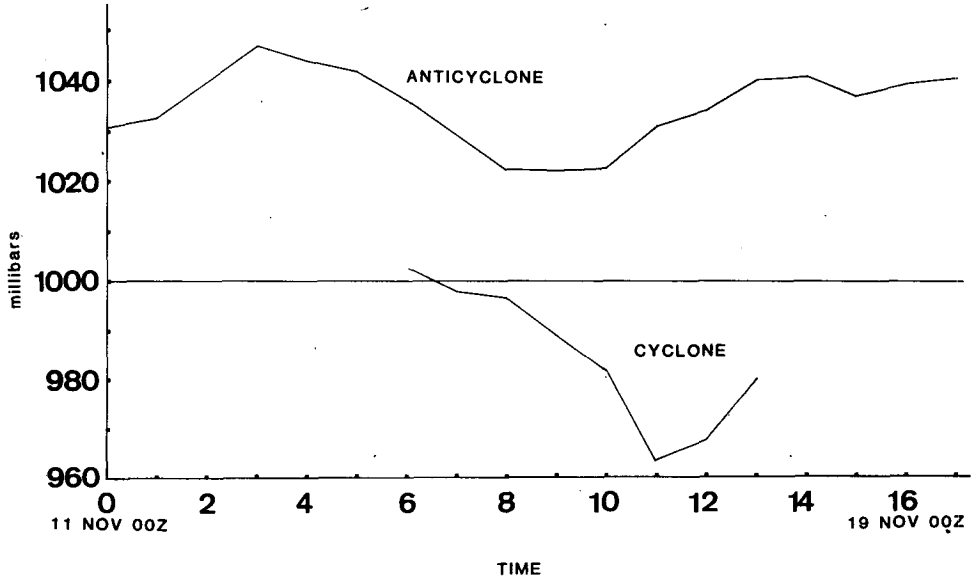

FIG. 1. Central pressure in millibars versus time period for the cyclone and anti-cyclone. Period 1 is 1200 GMT 11 November 1969 and period 16 to 0000 GMT 18 November 1969.

TABLE 1. Date time groups of time periods of case study.

Period	Date-time
1	1200 GMT 11 November
2	0000 GMT 12 November
3	1200 GMT 12 November
4	0000 GMT 13 November
5	1200 GMT 13 November
6	0000 GMT 14 November
7	1200 GMT 14 November
8	0000 GMT 15 November
9	1200 GMT 15 November
10	0000 GMT 16 November
11	1200 GMT 16 November
12	0000 GMT 17 November
13	1200 GMT 17 November
14	0000 GMT 18 November
15	1200 GMT 18 November

peak. Since period 1 this system has been intensifying and moving slowly eastward.

In period 3 a strong cyclone is present in the Gulf of Alaska. As the calculations presented in the next section show, this feature strengthens the upper level ridge to the west of the surface anticyclone mainly through low level warm advection. The cold air inland at lower levels is largely protected from this warm air by the Alaskan Range along the southern coast of Alaska. At this time the anticyclone is a shallow feature and is not evident as a closed circulation at 850 mb (not shown). As is typical of a cold anticyclone it is seen to be located on the cyclonic shear side of the polar front jet. This can be seen in Fig. 4 which is a cross section taken through the anticyclone and normal to the upper level flow.

By period 5 the anticyclone has decreased in central pressure and has moved slightly southeastward. Thickness contours indicate that cold air is spreading southward and that the anticyclone is taking on an elongated north–south configuration with strong flow indicated on the western and eastern flanks. From period 1, short waves, seen as isotach maxima at 300 mb, have been passing from the southwest to the southeast of the anticyclone and then into the central United States. These jet streaks have accompanied the push of cold air to the south. Another of these maxima can be seen just south of the anticyclone in period 5; it is this jet streak that the anticyclone follows in its move southward.

During periods 3 to 5 the 300 mb ridge to the west of the anticyclone has been building presumably in response to the warm advection in the Gulf of Alaska and over British Columbia. Concurrently as the cold air surges into the Northern Great Plains, there is strong trough development at 300 mb. The 864 dam contour forms a cutoff and drops rapidly southward from time period 3 to 5.

By period 7 the anticyclone has moved rapidly southward. The southern extent of a strong thickness gradient indicates that considerable cold air has penetrated as far as the Gulf of Mexico; this cold outbreak is accompanied by a strong isotach maximum at 300 mb. At this time the cyclone is indicated as being east of Norfolk, Virginia. It is not a distinct system in Fig. 2c but the NMC surface hand analysis shows a separate low pressure where the cyclone position is indicated. The cyclone windfield (not shown) gained a distinct circulation in period 6 off the Carolina coast and then deepened slightly and moved northward.

The isotach maximum at 300 mb is on the eastern side of the deep 300 mb trough by period 9. In response to this intense feature the 1000 mb cyclone has begun to deepen more rapidly. The cold air has made its farthest southward excursion by this period and the anticyclone has spread out along the Gulf coast.

By period 11 the anticyclone has moved up off the Carolina coast and has begun to re-intensify. The cyclone has developed to its lowest pressure of 964 mb. The cold dome is now actively subsiding as can be seen for example by the retreat of the 546 dam thickness contour to the north. Note that a lee cyclone has formed in the central United States, and in response to the warm advection west of the Great Lakes ridging is taking place aloft. The long wave trough in evidence over the Eastern United States in period 9 has been replaced by a sharp short wave ridge in just 24 hours.

By period 13 the cyclone center has been allowed to move off the analysis grid since interest for this case centered on the re-intensification of the anticyclone. The anticyclone has moved northward along the East coast and has strengthened considerably to its highest pressure since period 3. The 300 mb ridge to the west of the surface anticyclone is still being developed by the lower level warm advection now just over the Great Lakes.

Across the time span from periods 1 to 15 the anticyclone structure undergoes substantial changes. Figure 5 is a time cross section of potential temperature constructed from soundings closest to the center of the surface anticyclone for each period indicated. Considerable changes in vertical structure are evident, and the significance of these changes as the anticyclone changes from a cold, polar system in Alaska to a warm dynamic system off the East coast will be discussed in the next two sections. As seen in Fig. 2 the anticyclone during the time covered by this study has a tendency to move from the cold side of the thickness gradient toward the warm side. This is consistent with the fact that as the anticyclone becomes a warm core system it shifts from the cyclonic to the anticyclonic shear side of the jet stream. The opposite tendencies are observed for the cyclone as it develops toward occlusion.

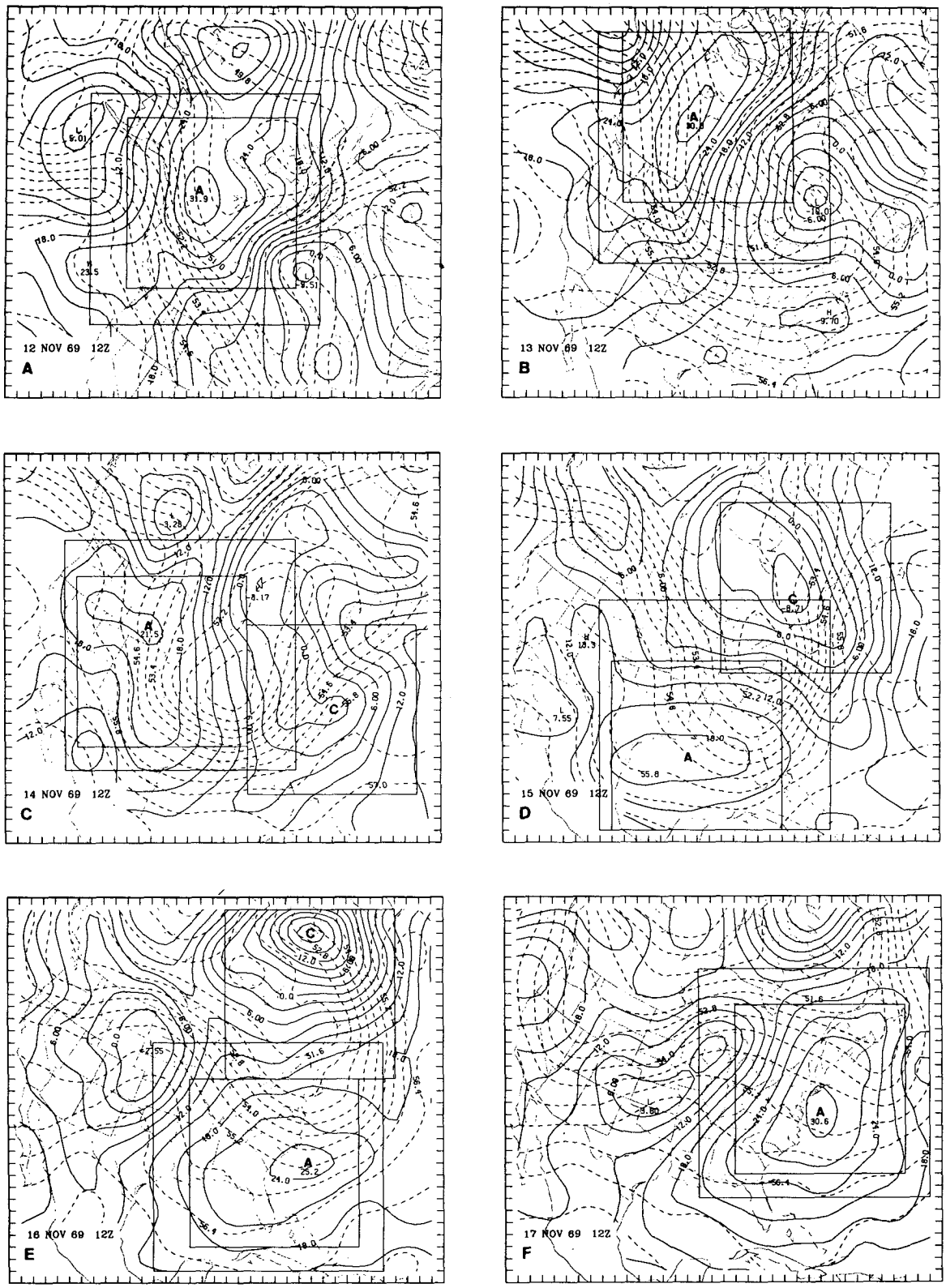

FIG. 2. (A), (B), (C), (D), (E), (F): 1000 mb height contours at 30 m intervals (solid) and 1000–500 mb thickness contours at 60 m intervals (dashed) for periods 3, 5, 7, 9, 11, and 13. Boxes indicate the volumes used in the energy budget calculations.

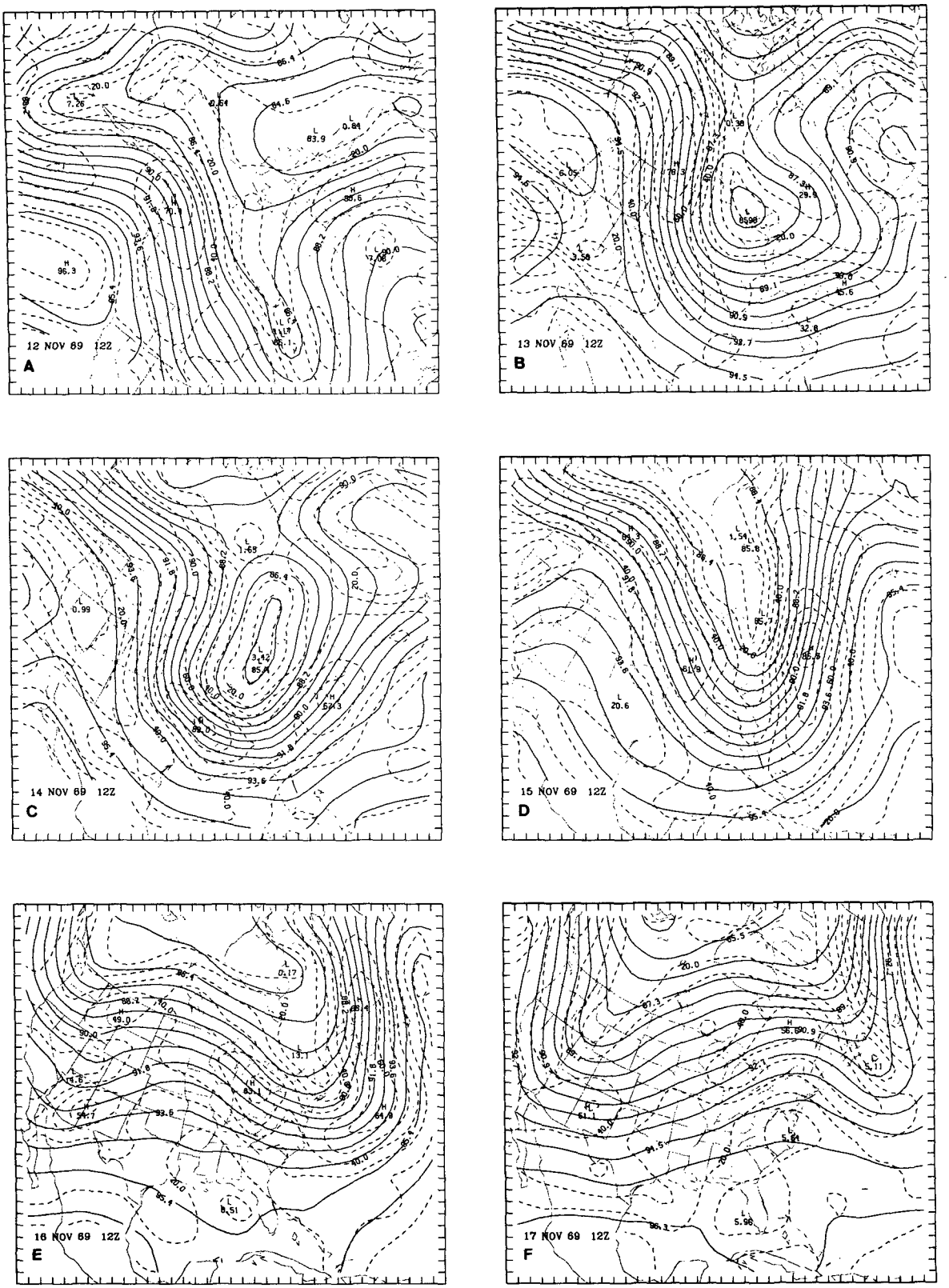

FIG. 3. As in Fig. 2, but for 300 mb heights at 60 m intervals (solid) and isotachs at 10 m s^{-1} intervals (dashed).

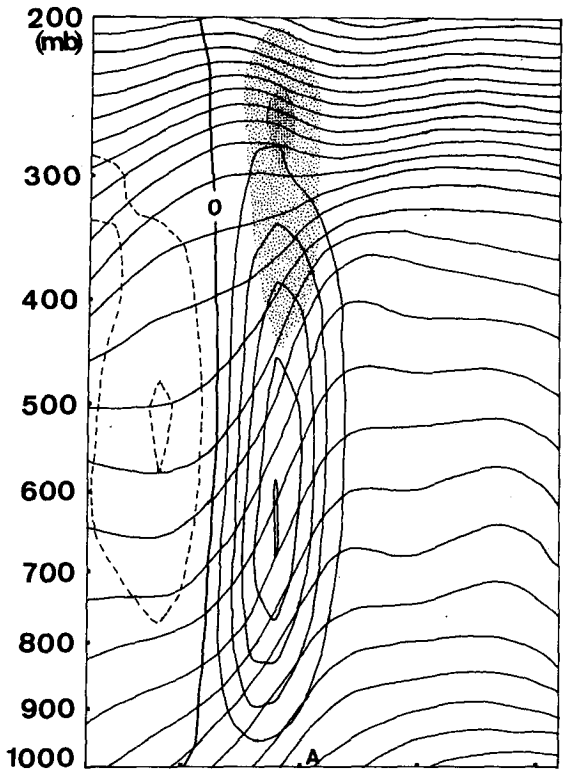

FIG. 4. Cross section of potential temperature and Quasi-geostrophic omega taken perpendicular to 500 mb flow through the position of the 1000 mb anticyclone for period 1. Contours are 4 K for isentropes, 0.1 Pa s^{-1} for omega. The inner and outer stippled areas are wind speed greater than 35 and 25 m s^{-1}, respectively. The A is position of the 1000 mb anticyclone center.

4. Quasi-geostrophic calculations and results

a. Quasi-geostrophic theory

In deriving the equations used in the isobaric calculations the formulation presented by Krishnamurti (1968) was followed. In his work the equation for omega ($\omega \equiv dp/dt$) was part of a set for a fully nonlinear balance model, and the equation contained twelve forcing functions. If we retain his first two forcing functions we arrive at the following equation for ω.

$$\nabla^2(\sigma\omega) + f^2\frac{\partial^2\omega}{\partial p^2} = \underset{\omega_v}{f\frac{\partial}{\partial p}[J(\psi, \eta)]} + \underset{\omega_T}{\pi\nabla^2 J(\psi, \theta)}, \quad (1)$$

where

σ stability parameter, $-(RT/p\theta)(\partial\theta/\partial p)$

η absolute vorticity

θ potential temperature

ψ rotational streamfunction

π $RT/(p\theta)$.

The streamfunction derivatives (ψ_x, ψ_y) were obtained from the analyzed wind components using the iterative technique of Endlich (1967). The values for potential temperature were derived from the analyzed temperature fields. Eq. (1) was solved using Liebmann successive over-relaxation. The boundary conditions were set so that ω was zero at 1000 mb

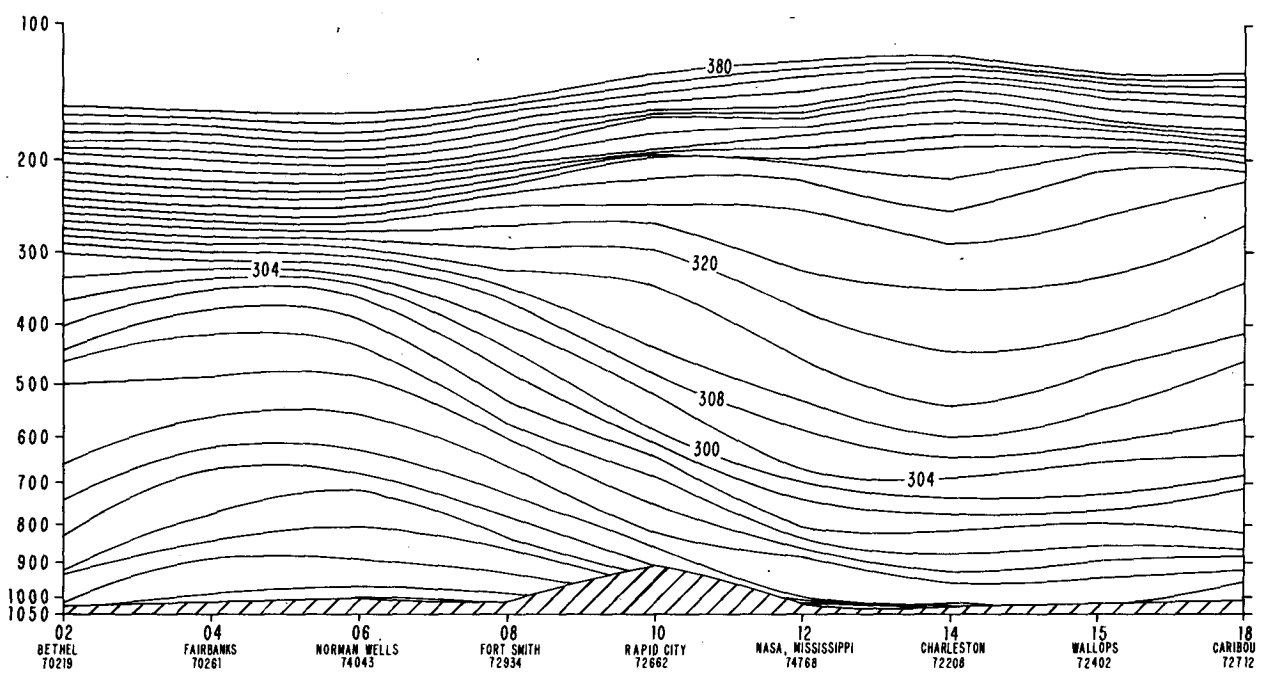

FIG. 5. Time section of potential temperature (K) versus pressure (mb) to the (R/c_p) for 1200 GMT soundings taken close to the anticyclone center.

and 100 mb, and on all horizontal boundaries. Omegas were computed every 100 mb from 900 mb to 200 mb.

It should be noted that by using the observed temperatures and rotational wind, Eq. (1) does not correspond to the classical QG omega equation such as presented by Holton (1979). In using the rotational wind (rather than the geostrophic) we are attempting to include the additional information that may be in the analyzed wind field. In the classical QG omega equation only data regarding the mass field (ϕ) is utilized. This rotational formulation of the omega equation, while it is a slight improvement over the classical QG form, is still a relatively low order (in Rossby number) approximation to the primitive equations. Therefore for simplicity the dynamics described by Eq. (1) will be termed quasi-geostrophic.

Note that since Eq. (1) is linear it can be solved separately for each of the forcing functions on the rhs. The contribution to the total ω due to the laplacian of thermal advection ω_T and differential vorticity advection ω_v can each be calculated. It is well known that the terms involving ω_T and ω_v contain a common factor and thus tend to have a large degree of cancellation between them, see e.g. Trenberth (1978), Hoskins and Pedder (1980), Hoskins *et al.* (1978). Nonetheless separating the field in this manner yields two forcing functions associated with processes regularly considered by synoptic meteorologists, i.e. vorticity and thermal advection. Various other formulations, Hoskins and Pedder, may yield equations more amenable to fast qualitative assessment by the forecaster examining synoptic charts, but these do not provide increased insight for quantitative calculations.

Once the fields of ω are determined, the geopotential tendency ($\partial\phi/\partial t \equiv \chi$) can be obtained directly from the vorticity equation:

$$\nabla^2\chi = -fJ(\psi, \eta) + f^2\frac{\partial\omega}{\partial p}. \qquad (2)$$

Using the partitioned omegas the contributions of each omega (ω_T, ω_v) to the geopotential tendency can be determined (χ_T, χ_v). Eq. (2) is solved using relaxation with χ being set to zero on all the horizontal boundaries.

The height changes corresponding to the fields of omega cannot be visualized easily by two dimensional charts of omega. Eq. (2) yields a picture of the effect of the vertical motion on the height field. Use of Eq. (2) rather than the classical QG height tendency equation (Holton, 1979), avoids having to specify the lower and upper boundary conditions on χ. Note that χ_T (χ_v) is the height change computed by neglecting the first term on the rhs of Eq. 2 and using ω_T (ω_v) in the second term.

b. Quasi-geostrophic results

1) ANTICYCLONE

Fig. 6a is a time series of ω_T and ω_v at 700 mb. The values are 4 point averages of a grid square centered on the 1000 mb anticyclone. Fig. 6b is a time series of χ_T and χ_v at 900 mb averaged over the same area as the omegas. Also included in Fig. 6b is the total height tendency at 900 mb; this is the sum of the previous two, plus that forced by vorticity advection, cf. Eq. (2). The 900 mb χ-fields are used since this level was the closest to the surface when solving Eq. (2). Fig. 6c is a time series of 700 mb ω_v and ω_T four-point averages at the position that the anticyclone will occupy 12 h hence.

Figs. 6a, b show that both the ω_v and χ_v terms play an important role in developing descent and height rises over the anticyclone in Alaska and the Northwest Territories (periods 1–4). Figs. 2 and 4 indicate that during these periods the anticyclone is located on a strong thermal gradient, and Figs. 6a, b show that the ω_T, χ_T terms also aid the anticyclogenesis at least in periods 1 and 2. The strength of the height rises in the initial periods is due to the superposition of these two basic forcings as the development begins.

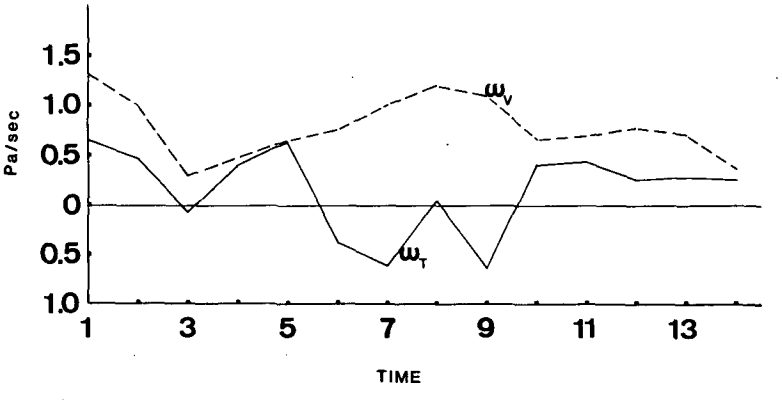

FIG. 6a. Time series of ω_T and ω_v at 700 mb. Values are four-point averages of a grid centered on the anticyclone. Units are Pa s^{-1}.

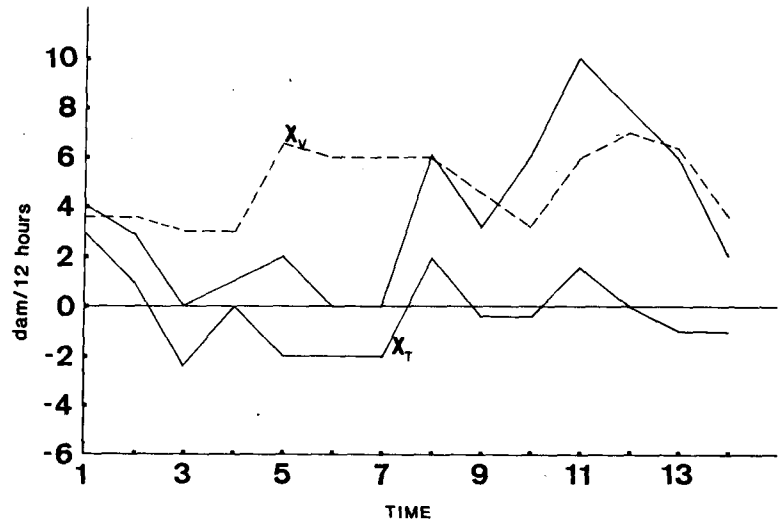

FIG. 6b. As in 6a only for X_v, X_T and X_{TOTAL} at 900 mb. Units are dam (12 hours)$^{-1}$.

It should be realized that while polar anticyclones are often referred to as shallow features, Fig. 4 illustrates the fact that subsidence associated with the anticyclogenesis extends throughout the entire troposphere.

Figs. 6a, c shed some light on the mechanisms for the anticyclonic movement as it proceeds southward to the Gulf coast during periods 5 to 8. It appears that the vorticity forcing is strongest over the anticyclone center acting to maintain the circulation (Fig. 6a) while the cold advection (thermal forcing of Fig. 6c) tends to precede the anticyclone. This is the well-known thermal "steering" mechanism of QG theory which is more often applied to cyclone movement. This concept of cold advection to the southeast acting as a steering mechanism for the anticyclone was described for a composite anticyclone by Dallavalle and Bosart (1975), based on an original concept described by Austin (1947). Figs. 7a, b for period 7, illustrate this effect by the two descent centers of ω_T and ω_v over the Great Plains. The ω_T center is somewhat farther south and indicates the location towards which the anticyclone is moving.

The anticyclone attains its southernmost position during period 9. As the anticyclone begins to ridge up along the east coast and re-intensify, the previous pattern of thermal forcing leading the vorticity forcing reverses. Fig. 6c for periods 10 to 13 clearly shows that the vorticity contribution to descent now is leading the movement of the anticyclone. This can also be seen by comparing the panels of Fig. 7 in the region of the anticyclone. Notice in period 10, Figs. 7c, d, the dominance of ω_v in the New York and Pennsyl-

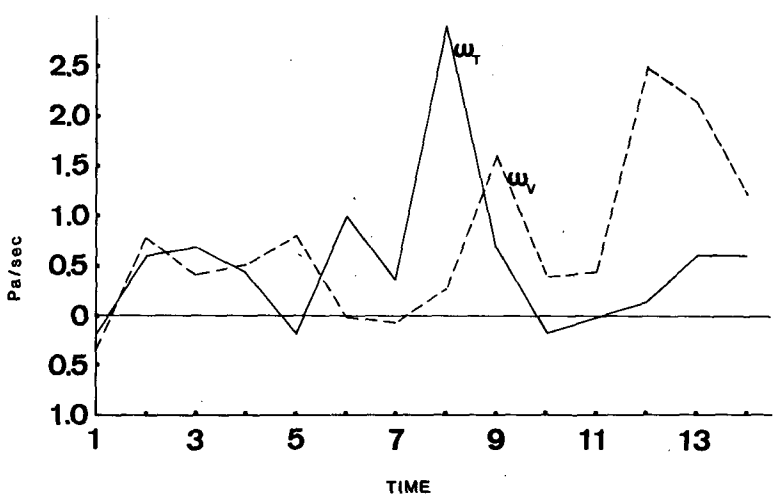

FIG. 6c. As in 6a only for the position that the anticyclone will occupy twelve hours hence.

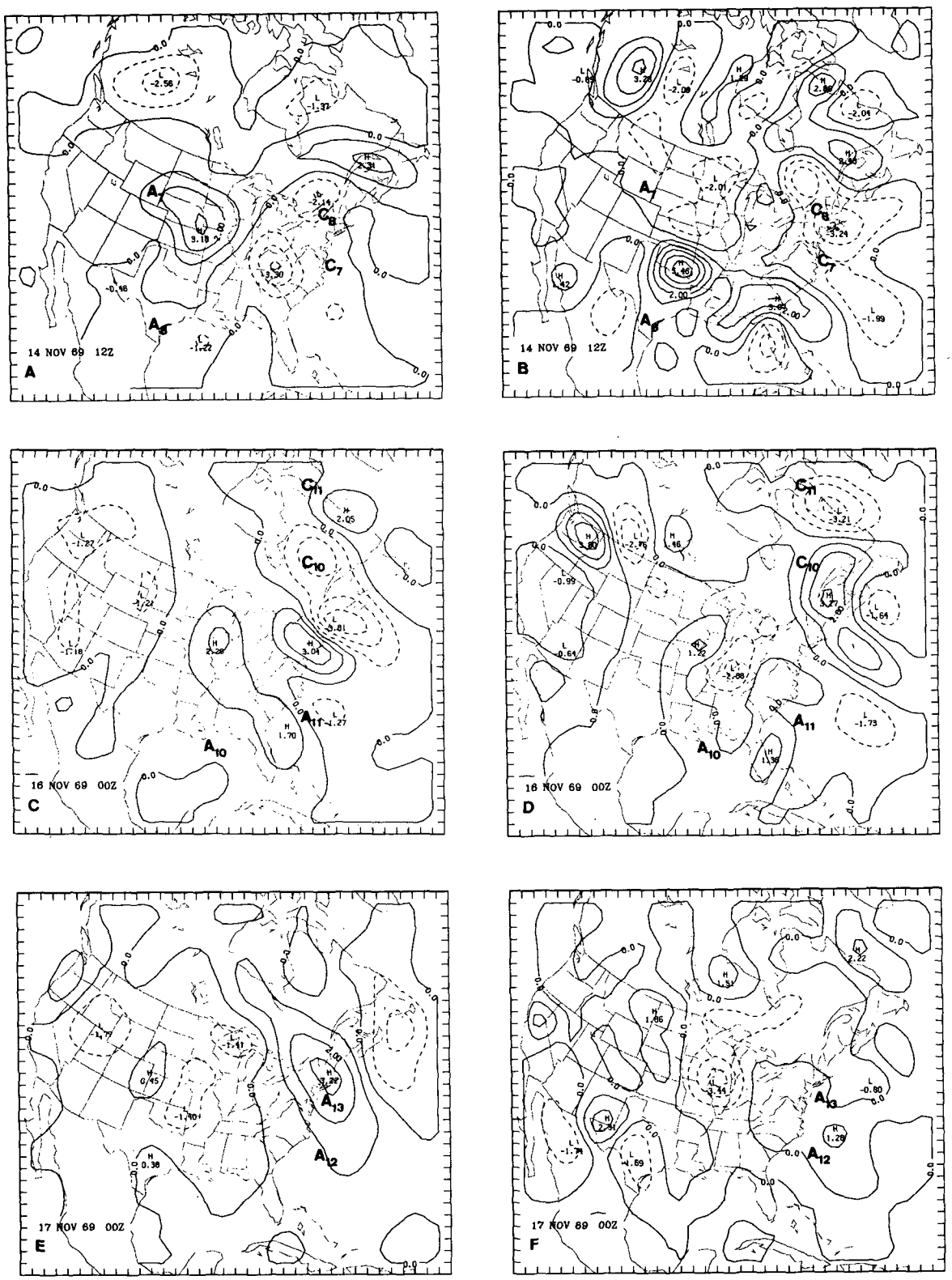

FIG. 7. The omega fields, ω_v at 700 mb (A), for period 7, (C) and (E) 10 and 12 and ω_T at 700 mb for (B), (D) and (F) periods 7, 10 and 12. Contour interval is 0.1 Pa s^{-1}. Positions of the anticyclone and cyclone are indicated for the present and succeeding time period.

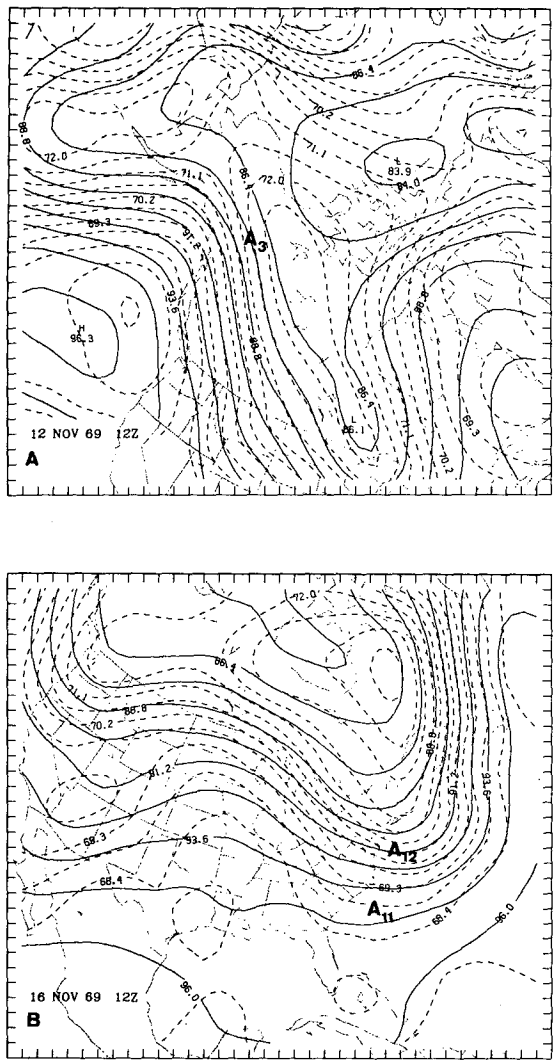

FIG. 8. The 100–300 mb thickness (contour interval 45 m) and 300 mb heights (contour interval 120 m) for (A) period 3 and (B) period 11. The 45 m contour interval corresponds to a mean column temperature difference of 1.4 K. The positions of the anticyclone are indicated.

vania region; this is a precursor of the pattern seen in period 13. By period 11 (Fig. 8b) the formation of a 300 mb ridge upstream from its later position near the Appalachian Mountains coupled with a weakened thickness gradient are indications of the ascendency of the hydrodynamic forcing as a steering mechanism. Pertinent to this change-over in dominant steering is the destabilization of the mid and upper troposphere together with stabilization of the lower troposphere indicated in Fig. 5. This change in structure by period 9 allows the upper level forcing (vorticity advection) to have a closer coupling to the lower level circulation (Holton, 1979). The lower values of stability mean that larger vertical displacements are required to effect the adiabatic temperature adjustments needed to maintain hydrostatic equilibrium. Thus the vertical motion is larger and of greater vertical extent in the regions of reduced stability, this yields a closer relation between lower level development and upper level (in this case vorticity advection) forcing.

Fleagle (1947) studied the evolution of a cold polar anticyclone to a warm system. He noted a "cap" of relatively cold air in the ridge aloft to the west of the surface anticyclone. The process of anticyclogenesis resulted in the cold cap and ridge both moving over the position of the surface anticyclone. Bodurtha (1952) also strongly emphasized the role of cold advection at 200 mb downstream of the upper level ridge in contributing to anticyclogenesis. He observed in cases of Alaskan anticyclogenesis that warm advection in the lower to mid troposphere to the west of the anticyclone forced an upper level ridge. The ascent in the upper troposphere and low stratosphere produced a pool of cold air aloft in the ridge, this cold air resulted in cold advection and subsidence downstream over the anticyclone. Figs. 8a, b are charts of the 300–100 mb thickness and the 300 mb height contours for periods 3 (1200 GMT 12 November) and 11 (1200 GMT 16 November). During period 3 the ridge along the coast of British Columbia and into Alaska is providing a source of upper level cold air which is being advected over the position of the surface anticyclone (see Fig. 2a). The cold advection results in large ($\sim$0.3 Pa s^{-1}) subsidence values due to ω_T at 300 mb (not shown). As the anticyclone proceeds southward this upper level cold advection abates (not shown). By period 11 the anticyclone is moving northeastward and reintensifying. From Fig. 8b it is clear that ridging to the west is resulting in strong cold advection along the middle Atlantic coast. However, even after the anticyclone has completely transformed to a warm, dynamic system the ridge and the cold air at high levels are not observed to become vertically aligned over the surface system. Consistent with Bodurtha's model of Alaskan anticyclogenesis, for the entire period of intensification along the East coast the anticyclone remains to the east of the coldest air aloft and tends to move toward the center of maximum cold advection at 300 mb.

2) CYCLONE

The development and intensification of the cyclone conforms reasonably well to standard QG theory. As seen by Figs. 1, 2 and 3 for periods 7 to 11, the cyclone only progresses to a well defined circulation after the upper level jet streak enters the 300 mb trough, seen as the wind speed maximum over Louisiana in Fig. 3c. The short wave triggers the cyclonic deepening by sharply increasing the differential vorticity advection. The process described above is a familiar type of cyclogenesis and is fully described by Palmen and Newton (1969) and Petterssen (1956).

Figs. 7a, b show that the ω_v ascent maximum is still slightly to the west of the cyclone center, while the ω_T ascent center is to the northeast during period 7. This is the manifestation of the thermal steering mechanism for a cyclonic system. Figs. 7c, d show the omega fields for period 10 prior to rapid (18 mb 12 h^{-1}) cyclonic development. The ω_v ascent maximum is close to the cyclone position. Note, from Fig. 3, that the cyclone is deepening while under the forward left divergent quadrant of the jet streak at 300 mb. Neglecting curvature effects this can be a favorable location since it is a region of ascending motion and dynamic destabilization both of which are the result of indirect circulation at the exit region of the jet streak (Uccelini and Johnson, 1979). Notice that there are two ω_v ascent centers near the cyclone in Fig. 7c. One is over the Bay of Fundy and can be attributed to effects of the longer wave trough (curvature vorticity). The other is near the cyclone center on the lhs of the jet streak exit region (shear vorticity). This illustrates the evidently important effect this very strong jet maximum exerted on the cyclonic development.

3) SENSIBLE HEAT EFFECTS

As outlined by Petterssen (1956) a diabatic heating maximum at the surface forces a center of height falls. The coastlines along the eastern and Gulf coasts become regions of such heating maxima during early winter as cold air comes off the continent over the relatively warm ocean. The purpose of this section is to evaluate the effects of sensible heating on the movement and development of the cyclone and anticyclone. Sensible heat fluxes between the ocean and air were computed for periods 6 to 13 of the present case.

The sea surface temperature (SST) analysis for this computation was subjective and based on ship reports from all time periods, the ocean temperature being considered fairly constant over the 5 days. Since the reporting ships were not distributed evenly over the region, climatological monthly mean values were combined with the observed values to provide a smooth transition in the analysis from data-rich to data-sparse regions. The method used to compute heat fluxes was a bulk aerodynamic technique developed by Kondo (1975).

Of prime interest here is not the heat fluxes themselves, but the effects of the flux on the 1000 mb height field. From Danard and Ellenton (1980) we have the following relation (their Eq. 19):

$$\frac{\partial}{\partial t}\zeta_{00} = \frac{R}{2f}\nabla^2\int_{p_{ND}}^{p_{00}}\left(-\frac{Q}{c_p}\right)d\ln p,$$

where

$$Q = g\frac{\partial H}{\partial p} = g\frac{(H_{00}-H_{ND})}{p_{00}-p_{ND}} = g\frac{H_{00}}{\Delta p}$$

and

p_{00} = 1000 mb,
p_{ND} = pressure at the level of non-divergence.

We have assumed that the sensible heat flux H is zero at p_{ND} and that sensible heat is convectively mixed to the level of p_{ND}. Now we make the QG assumption:

$$\zeta_{00} = \frac{g}{f}\nabla^2 Z.$$

Thus

$$\nabla^2\left(\frac{\partial Z}{\partial t}\right) = -\frac{R}{2c_p}\nabla^2\int_{p_{ND}}^{p_{00}}\frac{H_{00}}{\Delta p}\,d\ln p$$

or approximately:

$$\nabla^2\left(\frac{\partial Z}{\partial t}\right) \approx -\frac{R}{2c_p}\frac{\ln(p_{00}/p_{ND})}{\Delta p}\nabla^2 H_{00}. \qquad (3)$$

From the omega calculations a reasonable value for the level of non-divergence is about 500 mb. Thus, given the surface sensible heat flux, H_{00}, we can roughly estimate the height tendencies diabatically forced at 1000 mb by solving Eq. 3.

From Fig. 2d one can see that the cold advection off the coast of the Carolinas is intense for period 9, the magnitudes of heat fluxes are largest in this region as the cold continental air flows over the warm Gulf Stream. Maximum values are in excess of 300 W m^{-2}. Values of this magnitude are well in line with previous investigations of similar types of systems, (Kondo, 1975, Petterssen *et al.*, 1962, Gall and Johnson, 1977). These diabatic effects should inhibit further movement of the anticyclone northward along the coast. Notice that at this time (Period 9) Fig. 5 shows that the lowest 100 mb is nearly dry adiabatic as the sensible heat flux destabilizes the boundary layer at the offshore locations. The maximum of the QG forced 900-mb height rises is almost coincident with the diabatically forced 1000-mb height falls. The magnitude of the QG height rises are almost *five times* the falls due to sensible heat flux (80 versus 17 m 12 h^{-1}). Therefore, the diabatic height falls are overwhelmed by the QG height rises and the anticyclone moves northeastward along the coast despite opposition by the sensible heat forcing. The pattern of the other time periods is similar.

The sensible heat flux might also contribute to the developing warm core structure of the anticyclone. However, Fig. 5 shows that this heating is restricted to the very lowest levels and does not impact the deeper thickness changes. The soundings of Fig. 5 are over land, but the analyses show that similar conditions are prevalent over water.

5. Potential vorticity

Eliassen and Kleinschmidt (1957) relate masses of high potential vorticity (PV) air aloft to surface cy-

clones where here we are referring to the approximation to the potential vorticity defined by (Staley, 1960):

$$P = -g\frac{\partial\theta}{\partial p}(\zeta_\theta + f), \tag{4}$$

where the θ subscript implies that the relative vorticity is calculated on an isentropic surface. In their simple model the presence of high values of potential vorticity aloft will force a cyclonic circulation at the same level as the mass itself. If the surface potential temperature is uniform a surface cyclone will be located directly below the potential vorticity maximum (PVM). The isentropic surfaces below the mass will be raised locally; thus the cyclone is a cold core system.

In his numerical experiments, Bleck (1973, 1974) was able to take a somewhat more realistic approach than that of Eliassen and Kleinschmidt. Bleck's model was based on the conservation of potential vorticity on isentropic surfaces. He showed that the stretching of vortex tubes is most intense whenever high potential vorticity air aloft experiences a depletion of isentropic coordinate surfaces beneath it. This occurs when the PVM aloft passes from the cold to the warm side of a surface front. In a dry model based on potential vorticity conservation, vortex tube stretching is the sole vorticity producing mechanism. Since the lower boundary is not one of uniform potential temperature, the PVM aloft is shifted towards the cold side of the baroclinic zone with respect to the surface front.

Fig. 9 displays the potential vorticity [Eq. (4)] interpolated to the 500 mb pressure surface for time periods 7–11. The 2×10^{-7} K m^2 s^{-1} kg^{-1} contour has been emphasized. This value of PV is frequently taken as a rough dividing line between stratospheric and tropospheric values of potential vorticity (Danielsen and Hipskind, 1980). Air having values greater than this is generally considered to have a stratospheric origin. Fig. 10 is the potential vorticity on the 300 K isentropic surface for periods 9 and 11. Selected isobars are also shown.

Comparing the PV values on the 300 K surface for periods 5–9 (not shown) with the thickness contours in Fig. 2, it is found that extension of the strong thickness gradient from Canada into the Central United States is accompanied by a mass of high PV air located on the cold side of the thickness gradient. As can be seen by comparing Figs. 10a and 2d, the lowest thickness contours provide a good guide to the location of the potential vorticity maximum (PVM) on the 300 K surface. The cold dome and the PVM centers nearly coincide, consistent with the static model of Eliassen and Kleinschmidt. The PVM at 300 K has its southernmost extension by period 8 (not shown) while for comparison the 546 dm thickness contour attains its farthest equatorward position during period 9. By period 9 the jet streak has passed to the eastern side of the trough (Fig. 3d), the cold air dome has begun to collapse and the PVM on the 300 K surfaces halts its southeastward advance and turns to the northeast.

The passing of the jet streak to the eastern side of the trough is reflected in the potential vorticity patterns of periods 7, 8 and 9 in Fig. 9. At the onset of cyclogenesis off the Carolina coast during period 7 the PVM center is well upstream. In the ensuing 24 h the slowly intensifying cyclone tracks northward and is located in eastern Canada. Simultaneously the PVM increases markedly as does the area encompassed by the 2.0×10^{-7} K m^{-2} s^{-1} kg^{-1} contour denoting stratospheric values. During these periods the PVM on the 300 K surface (not shown) displays a movement towards higher pressure (warmer air), and Fig. 9 (along with similar figures at 700, 600 and 400 mb, not shown) indicates that the high PV air is extruding downward from the stratosphere. These processes appear to be consistent with the mechanism outlined by Bleck (1974). After period 9 the values of PV at 500 mb begin to decline and the area enclosed by the P_T contour decreases. However at this time the cyclone at the surface is developing rapidly (Fig. 1). The fact that PV values at 500 mb (and levels above and below) begin to decrease while the storm continues to develop, indicates that the vortex stretching by the advection of high PV air is not the sole mechanism for increasing a cyclonic circulation. Evidently in this case diabatic effects play an important role. It appears from the sequence depicted in Fig. 9 that extrusion of high PV air towards the surface (high PV air being advected toward higher pressure on an isentropic surface) is an important factor in initiating the cyclone, but is somewhat less vital in the latter stages of development.

Note that during cyclogenesis, periods 7 and 8, the PVM at 500 mb is to the southwest and south of the developing cyclone, (Figs. 9, 2). (The PVM values at 300 K have roughly the same position with respect to the cyclone center.) The fact that the PVM at 500 mb is not directly above the cyclone at the surface can be attributed in part to the fact that the air below does not possess horizontally uniform potential temperature. Since the cyclonic development should proceed at this point where the maximum advection of PV on isentropic surfaces towards higher pressure occurs, the PVM itself will be positioned back towards the colder air.

In Fig. 10 the rapid decrease in the PVM from periods 9 to 11 is apparent, this decrease can also be seen in periods 10 to 11 of Fig. 9. Before these time periods, 9–11, the fields of PV on isentropic surfaces were fairly conservative in the sense that advection on the surface could account for the bulk of the changes in the fields. There was some variability in the maximum values which can be attributed to va-

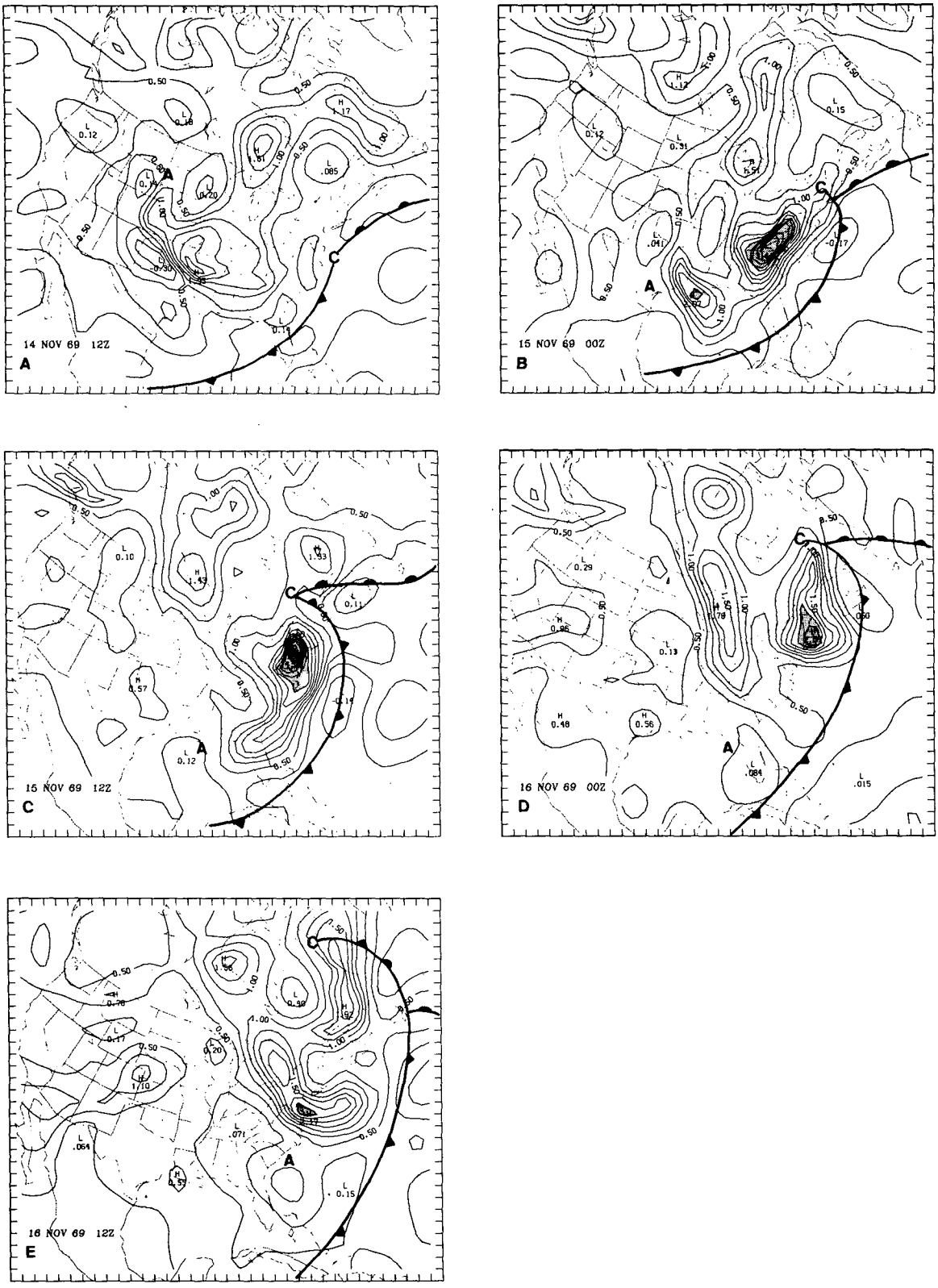

FIG. 9. Potential vorticity at 500 mb for (A)–(E) periods 7, 8, 9, 10, and 11, respectively. Contour interval is 2.5×10^{-7} K m^2 s^{-1} kg^{-1}. Regions with values greater than 2.0×10^{-6} K m^2 s^{-1} kg^{-1} are stippled. Surface frontal features and positions of the surface highs and lows are indicated.

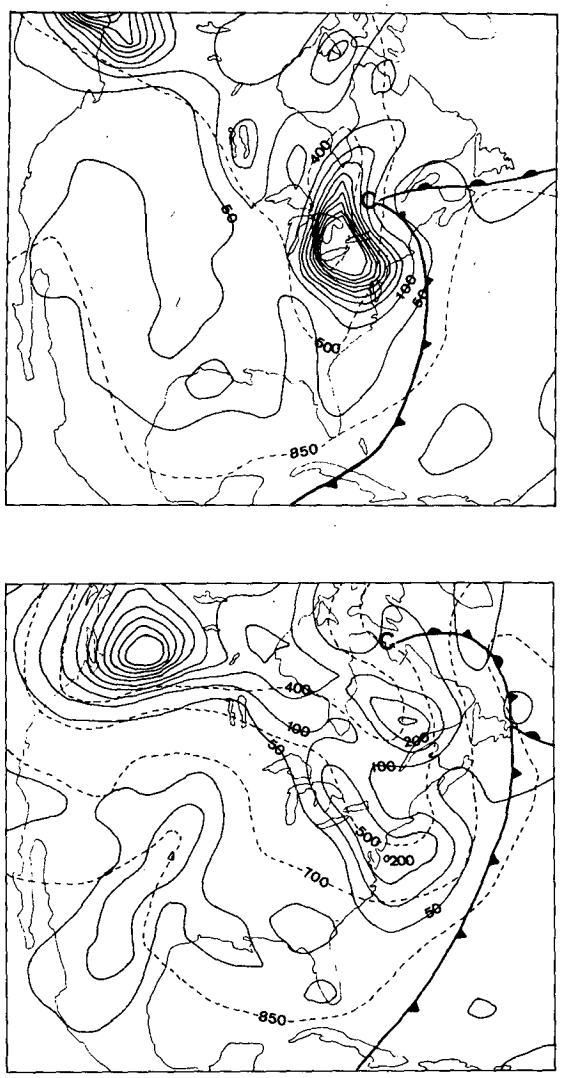

FIG. 10. Potential vorticity on the 300 K surface at intervals of 5.0×10^{-7} K m^2 s^{-1} kg^{-1} (solid) and selected pressure contours (dashed) for (A) period 9 (1200 GMT 15 November 1969) and (B) period 11 (1200 GMT 16 November 1969). The highest potential vorticity contour is 5.0×10^{-5} K m^2 s^{-1} kg^{-1}. Surface frontal features and positions of the surface highs and lows are indicated.

garies in the analyses and to vertical mixing by subgrid scale processes (Danielsen, 1968). Changes in potential vorticity given by Eq. (4), following the motion are given by:

$$\frac{dP}{dt} = \eta_\theta \frac{\partial}{\partial p}\left(\frac{d\theta/dt}{\pi}\right),$$

where

$\pi \equiv c_p(p/p_{00})^\kappa$,

$\eta_\theta = \zeta_\theta + f$,

c_p = specific heat of air at constant pressure.

We have neglected the product of the horizontal components of the vorticity vector and horizontal gradient of diabatic heating, and assumed frictionless flow, with no mixing.

The surface temperature field in the storm vicinity at occlusion is closer to a uniform potential temperature than it was at cyclogenesis. By the model of Eliassen and Kleinschmidt (1957) the surface cyclone and the PVM aloft should thus be more closely aligned vertically at occlusion. Thus, as the storm occludes the PVM moves closer to the center of the cyclone and there encounters the stronger gradients of condensational heating. Unfortunately the present data available does not allow for an explicit quantitative evaluation of the PV altering mechanism, so a definitive answer for this case must be deferred.

However, an estimate of the effect of the stable release of latent heat on the potential vorticity can be obtained from the results of Danard (1964). Danard has published figures of the distribution of heating due to latent heat release at various levels. Table 2 gives a summary of the Danard figures. This is for a precipitation rate of 0.3 mm h^{-1} [1.8 cm (6 h)$^{-1}$].

If we assume a modest value of $\eta_\theta \sim f$, we obtain a decrease in P of $\sim 2 \times 10^{-6}$ m^2 K (s kg)$^{-1}$ 12 h^{-1} $\sim 4.6 \times 10^{-11}$ m^2 K (s kg)$^{-1}$ s^{-1} which is the correct order for the changes observed at about 500 mb ($\sim$300 K surface above the cyclone).

Past work has concentrated on the cyclone's development in relation to upper level potential vorticity. Notice in Fig. 10 that for periods 9–11 a minimum in PV is developing in the southerly trajectory to the west of the building anticyclone (Fig. 2) along the east coast. The situation appears to be analogous to that discussed above for the cyclone. Note that here the PV minimum is located on the warm side of the thickness gradient from the anticyclone. However, the PV minimum is considerably more diffuse than the PV maximum. This is probably a reflection of the gradient wind constraint limiting the negative values of ζ_θ and the smaller values of $\partial\theta/\partial p$ in warm air. The result is that the anticyclone development is on a somewhat more modest scale and more diffuse than that of the cyclone. Also the thickness gradient is not as steep to the west of the anticyclone as it was for the cyclone (Fig. 2). A similar PV minimum was also seen to the west of the anticyclone, during period 1, when anticyclogenesis occurred over Alaska.

TABLE 2. Vertical gradients of heating due to condensation.

Level (mb)	Heating due to condensation H (m^2 s^{-3}) Danard (1964)	$H/c_p(p/p_{00})^\kappa$ (K s^{-1})	$\frac{d}{dp}\left(\frac{d\theta/dt}{\pi}\right)$ K s^{-1} (10^4 Pa)$^{-1}$
400	3×10^{-1}	3.9×10^{-4}	2.22×10^{-4}
500	5×10^{-1}	6.1×10^{-4}	
600	3×10^{-1}	3.5×10^{-4}	2.6×10^{-4}

6. Quasi-lagrangian kinetic energy budgets

The time rate of change of kinetic energy K, moving with a limited volume of horizontal cross section A and bounded by pressures p_1 and p_2 is given by Vincent and Chang (1973):

$$\frac{\delta K}{\delta t} = \frac{1}{gA}\int_A\int_{p_1}^{p_2}\Big[\underbrace{-\nabla\cdot(k\mathbf{V})}_{\text{BFLX}} + \underbrace{\mathbf{C}\cdot\nabla k}_{\text{CFLX}} \underbrace{-\frac{\partial(k\omega)}{\partial p}}_{\text{VFLX}} \underbrace{-\mathbf{V}\cdot\nabla\phi}_{\text{GEN}}\Big]dpdA + \underbrace{D}_{\text{RES}}, \quad (5)$$

where

$$\frac{\delta K}{\delta t} = \frac{\partial k}{\partial t} + \mathbf{C}\cdot\nabla k,$$

$$K = \frac{1}{gA}\int_A\int_{p_1}^{p_2} k dpdA, \quad k = \tfrac{1}{2}\mathbf{V}\cdot\mathbf{V},$$

$\mathbf{C}$ = velocity of the walls of the budget volume.

All terms, except term D which represents sub-grid scale processes (turbulence, friction), can be explicitly calculated from the analyzed variables u, v, and ϕ. Term D is calculated as a residual (RES), and thus not only contains true sub-grid scale effects but also errors involved in computing the other terms (Holopainen, 1973). In order to achieve consistency with virtually all previous KE budget studies, kinematic omegas were used in calculating the vertical flux term. The kinematic omegas were computed by vertically integrating the divergence obtained from the analyzed u, v wind components. The adjustment technique of O'Brien (1970) was used in its linear form to force omega to zero at 1000 and 100 mb. Budgets were also computed using Eq. (5) but for the divergent and rotational part of the wind separately. The wind was separated into rotational and non-divergent components using the iterative technique of Endlich (1967).

Two horizontal areas were used for the budget volumes, a 20 × 20 and a 15 × 15 subset of the analysis grid (~190 km grid length). Due to the size of the anticyclonic region both 20 × 20 and 15 × 15 grids were used for volumes following the anticyclone motion, for brevity these will be referred to as 20A and 15A. Only the 15 × 15 grid was used for the more compact cyclonic system, this will be referred to as 15C. The area encompassed by the 20 × 20 grid is about 14×10^{12} m^2 while that of the 15 × 15 grid is about 8×10^{12} m^2. These regions are indicated in Fig. 2.

The number of detailed KE budget studies that consider the anticyclonic region per se is not large. Kung and Baker (1975) present composite results of 420 cases. Chen and Bosart (1977) treated the KE budget of a composite anticyclone, while Smith (1973) presents about the only detailed KE budget of an individual anticyclone. In the following discussion the results will often be compared to those of Kung and Baker (1975), hereafter KB. Thus, it should be noted that KB use an Eulerian budget technique, with an area somewhat larger than the 15 × 15 grid.

Fig. 11 shows the results for 15A averaged over periods 1–7, times that cover the formation and movement of the anticyclone southeastward into the United States. The figure displays the vertical distribution of the quantities defined in Eq. (5) integrated over the 15 × 15 grid and a pressure interval of 100 mb. Notice that flux due to the volume movement (CFLX) is plotted separately from the boundary flux BFLX. A major drawback to QL budget studies is the ambiguity concerning physical interpretation of the CFLX term. We feel that it is not appropriate to present only that total of the CFLX and BFLX terms for this can obscure information that the BFLX values are providing. Positive (negative) BFLX values indicate that over the time periods considered KE is being imported to (exported from) the volume, while the CFLX term can vary depending upon the subjectively determined surface system velocity $\mathbf{C}$.

Fig. 11 indicates rather large cross-isobar flow and dissipation in the lowest layers, this is probably due to rather strong flow over rugged terrain (Fig. 2, period 5). The VFLX, RES and BFLX terms all behave with patterns similar to the KB average anticyclone, while the GEN and DKE resemble the KB cyclone pattern. Fig. 11 resembles the data from other KE budget studies of cyclones in that there is a balance

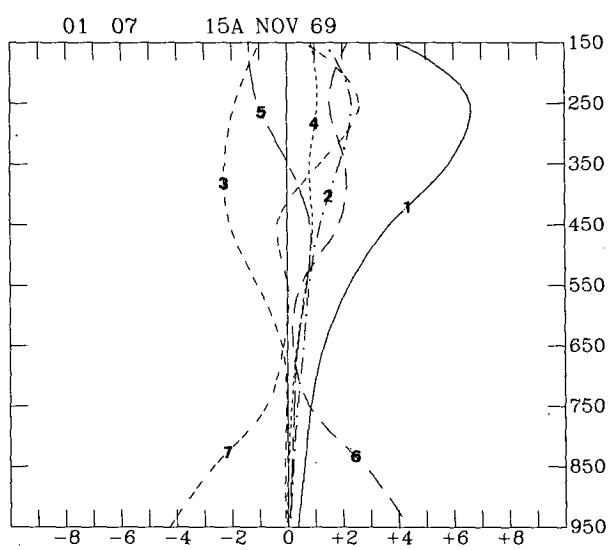

FIG. 11. Vertical profiles of kinetic energy budget terms. (1) Kinetic energy ($\times 10^5$ J m^{-2}). (2) Change of kinetic energy. (3) Horizontal flux. (4) Horizontal flux due to system motion. (5) Vertical flux. (6) Generation. (7) Residual for the 15 × 15 anticyclone region averaged for Periods 1 to 7. Units for (2) to (7) are W m^{-2}.

between generation and dissipation in the boundary layer with the dominant term being the BFLX or GEN at upper levels. Note the prominent role played by the VFLX term, this plays a greater role in our results than in KB and in most other studies. This probably can be attributed in part due to the smaller area of 15A compared to the KB region. The results of 20A for similar periods indicate a smaller role for the VFLX. Also, the QL nature of the budget keeps the volume over the center of most vigorous vertical motion, which tends to make the VFLX larger in QL budgets as compared to Eulerian ones.

Fig. 12 shows the results averaged over periods 6–9 for 15A. During this time the anticyclone moved from the middle of the United States to the Gulf Coast. Note the large VFLX term, this represents a major source of KE for the lower layers (below ~600 mb) evidently a large part of which is exported, as indicated by the BFLX. In Fig. 12 the GEN term pattern is similar to the KB cyclone results.

Fig. 13 shows the budget for volume 15A averaged over periods 8–11. The CFLX now plays a major role, this is due to a rather strong jet streak (60–70 m s^{-1}) which is located on the eastern edge of the 15A volume which is moving eastward following the anticyclone. It is during periods 8–11 that the cold dome collapses. Here the RES and GEN terms appear more like the KB cyclone pattern. Fig. 14 shows the GEN term for the rotational ($-\mathbf{V}_R \cdot \nabla\phi$), divergent ($-\mathbf{V}_D \cdot \nabla\phi$) and whole wind ($-\mathbf{V} \cdot \nabla\phi$). As in all periods the $-\mathbf{V}_D \cdot \nabla\phi$ term dominates in the boundary layer. The total GEN obscures a strong negative correlation between the generation due to the rotational and divergent wind. The chart of $\omega'\alpha'$ at 500 mb for period 8 (not shown) indicates a strong descent of cold air over the southeast United States. These facts suggest that part of the energy release of the subsiding cold

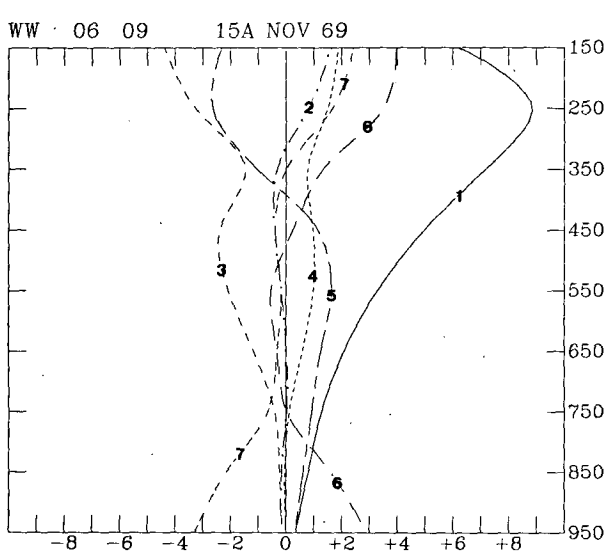

FIG. 12. As in 11 except averaged over periods 6–9.

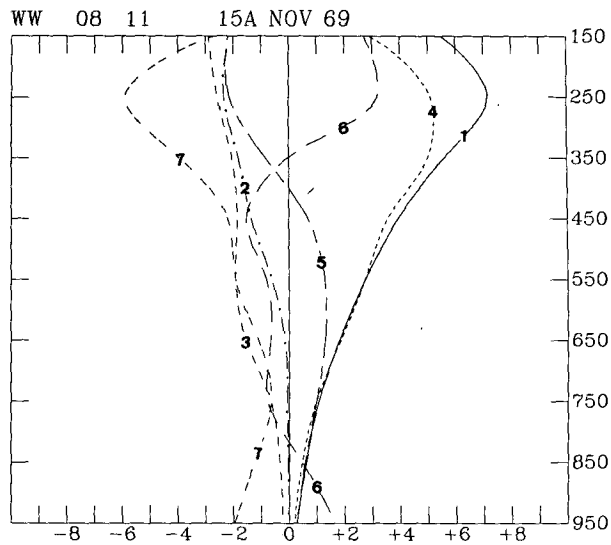

FIG. 13. As in 11 except averaged over periods 8–11.

air is reflected in the generation by the divergent component. It is tempting to suggest also that some of this energy (of the direct circulation) is then exported (export by work performed against the pressure gradient is dominated by the rotational wind) and augments the jet streak now to the northeast of the anticyclone.

The limited area averages of Fig. 14 can be misleading as to the larger scale processes at work. Figure 15 contains fields of the cross-contour flow ($-\mathbf{V} \cdot \nabla Z$) for the whole, rotational and divergent wind and the heights and wind speed for period 8 at 300 mb. The areas encompassed by 15A, 20A and 15C are

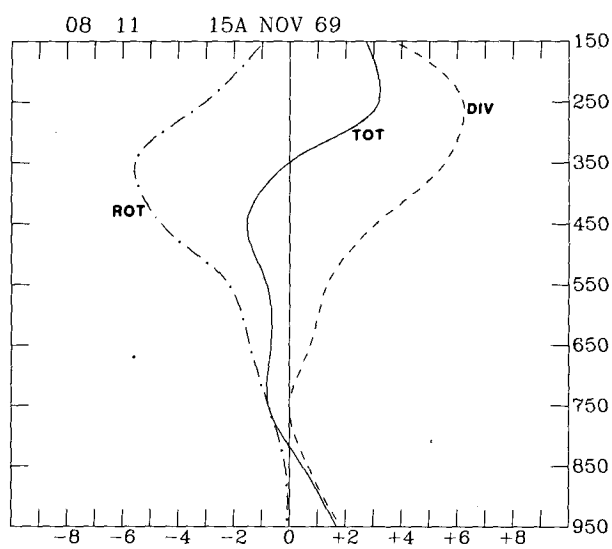

FIG. 14. Vertical profiles of the generation of kinetic energy by the divergent (DIV), rotational (ROT) and whole wind (TOT) for the 15 × 15 anticyclone volume averaged over periods 8–11. Units are W m^{-2}.

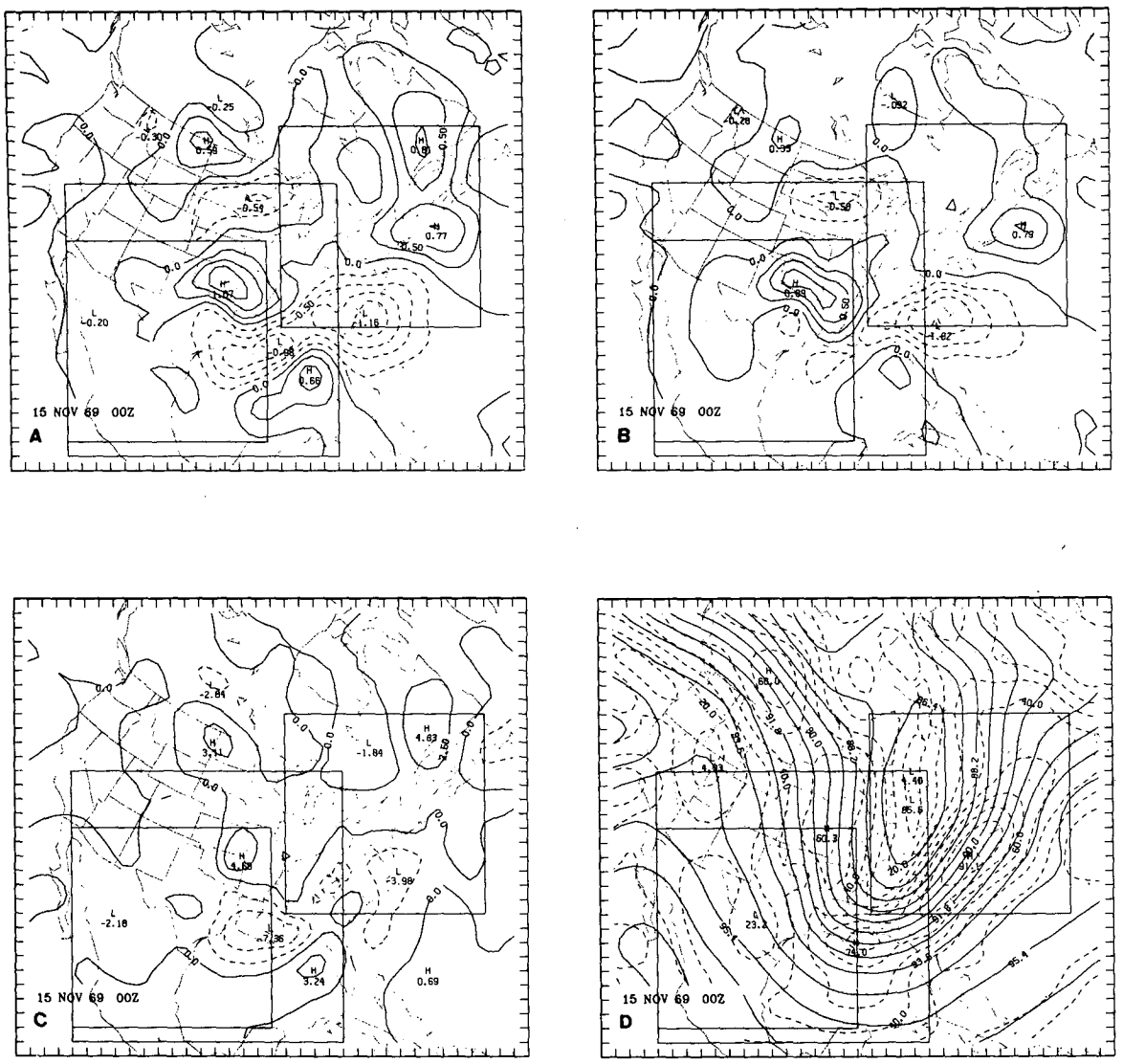

FIG. 15. Cross contour flow ($-\mathbf{V}\cdot\nabla Z$) for the whole (A), rotational (B) and divergent wind (C) for period 8 (0000 GMT 15 November 1969) at 300 mb. Contour interval is 2.5×10^{-3} m s^{-1}. Dashed contours indicate generation of kinetic energy, solid contours indicate destruction. (D) The 300 mb heights and wind speed for the same time as above. Contour intervals are 60 m and 10 m s^{-1}, respectively. Boxes indicate volumes used in the energy budget calculations.

also illustrated. Notice that the area of 15A is mainly one of rotational destruction and divergent generation of kinetic energy. The fields of Fig. 15 delineate two separate regions of strong cross-contour flow of the rotational wind. Krishnamurti (1968) showed that there is a substantial contribution to cross-contour flow by the rotational wind. He states that there is destruction of kinetic energy to the west of the major trough axis and generation to the east. This is also in evidence in Fig. 15b. Pearce (1974) indicated that in short waves (jet streaks) that there is generation in the entrance region and destruction in the exit region (his Fig. 9). This pattern is evident in Fig. 15b with the jet streak centered over Maryland. Pearce's (1974) results also show divergent generation on the warm side of the subsiding cold air mass, this is shown for the present case by the maximum along the Gulf Coast in Fig. 15c. It would thus appear that anticyclones which tend to be located to the west of the trough axis and toward the warm side of the cold air dome (west flank of cold air) would preferentially display generation profiles such as those in Fig. 14 as the cold air subsides.

The results for periods 10–15 for volume 15A are shown in Fig. 16. This is the time when the anticyclone establishes itself as a warm, dynamic feature off the east coast. The profiles are rather mixed with CFLX being the only clearly dominant term. There is a sharp decrease in the GEN term above 400 mb from Fig. 14. It is interesting to note that the synoptic

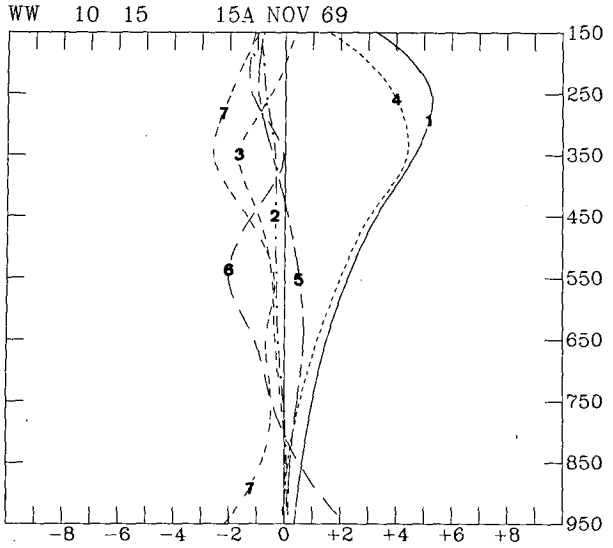

FIG. 16. As in 11 except averaged over periods 10–15.

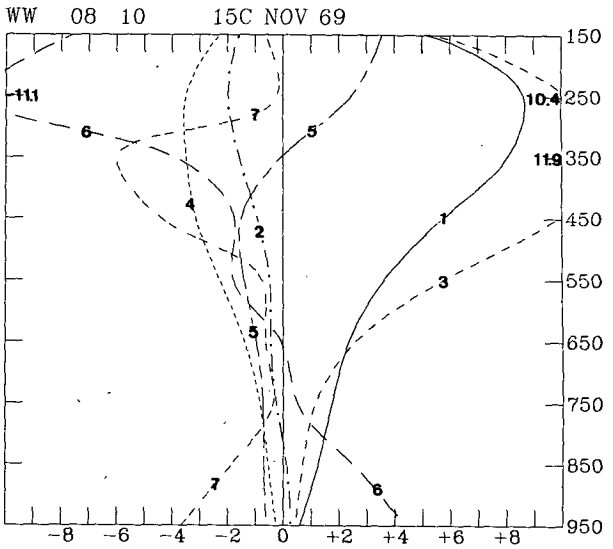

FIG. 18. As in 11 except for the 15 × 15 cyclone region averaged over periods 8–10.

situation of these periods is remarkably similar to that of the anticyclone for which Smith (1973) computed his KE budgets. His results were also rather unremarkable.

Due to the fact that the cyclone was allowed to pass off the analysis grid as it matured we can only consider the developing stages of the cyclone in the KE budget studies. Fig. 17 presents the budget for volume 15C for period 6–9. Again the VFLX term plays an important role. The dominant source of KE above the BL is the BFLX term similar to cyclone 1 of the Alpert (1981) study. Fig. 18 displays the results for periods 8–10, a time of steady (15 mb 24 h^{-1}) development. The BFLX term is overwhelmingly the largest source of KE above 700 mb, while the GEN is a source in the boundary layer and a sink at jet level. This destruction at jet level is dominated by the rotational component, $-\mathbf{V}_R \cdot \nabla\phi$ being three times as large as $-\mathbf{V}_D \cdot \nabla\phi$ (Fig. 19). Thus, we have a picture of divergent generation and export of KE in 15A while downstream in volume 15C are found rotational destruction and import of KE.

Fig. 20 provides graphs of the vertically integrated GEN and BFLX terms for volumes 15A and 15C for all periods for which budgets were calculated. As regards the role of these disturbances in the general circulation one should note that the global integral of $-\mathbf{V}_R \cdot \nabla\phi$ is zero while the value of the global integral of $-\mathbf{V}_D \cdot \nabla\phi$ is non-zero. Since the $-\mathbf{V}_D \cdot \nabla\phi$ totals are positive for all time periods, both volumes 15A and 15C contribute to the net generation of KE.

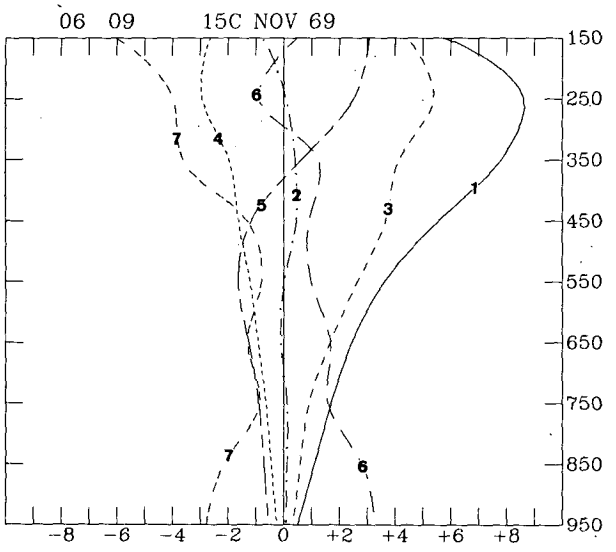

FIG. 17. As in 11 except for the 15 × 15 cyclone region averaged over periods 6–8.

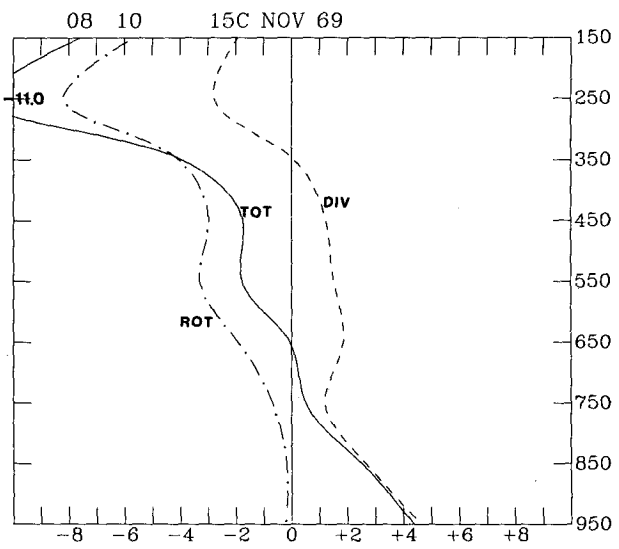

FIG. 19. As in 14 except for the 15 × 15 cyclone region averaged over periods 8–10.

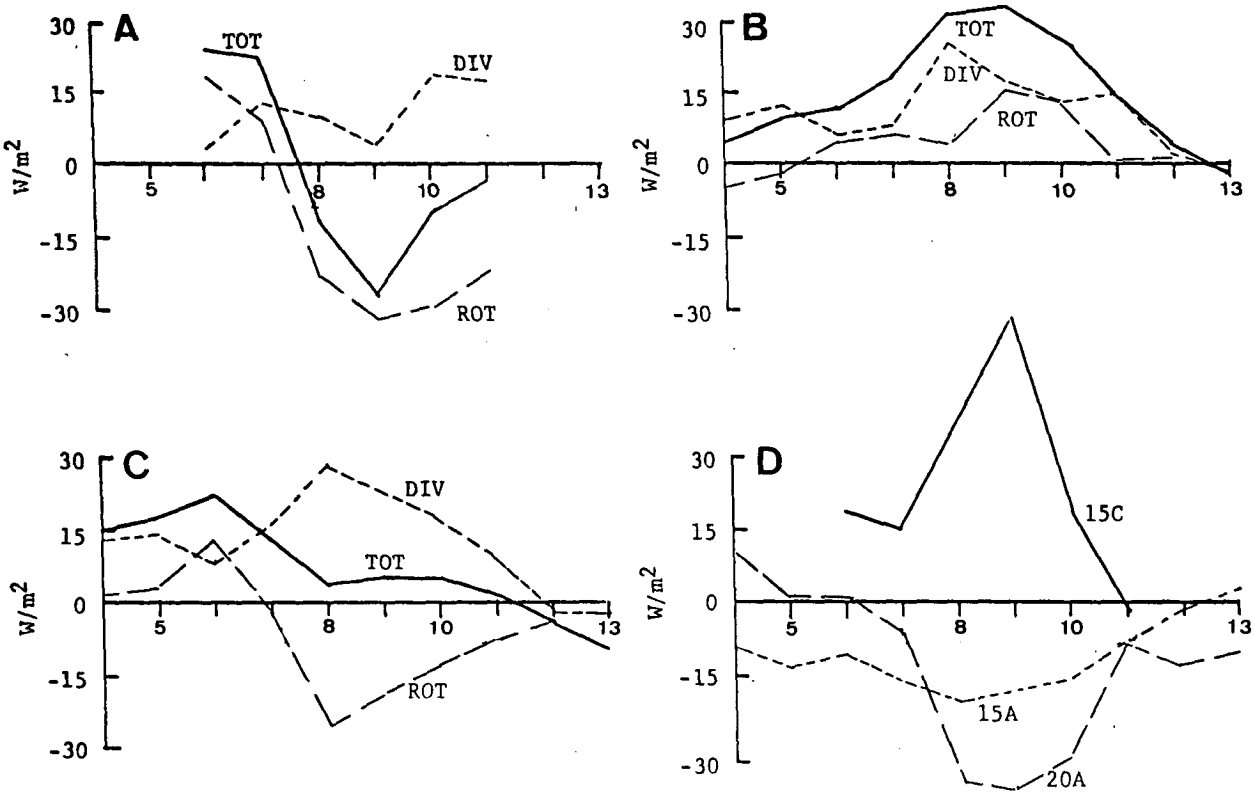

FIG. 20. Time series of vertically integrated kinetic energy generation for (A) the 15 × 15 cyclone volume, (B) the 15 × 15 anticyclone volume and (C) the 20 × 20 anticyclone volume for both the whole, rotational and divergent wind. (D) presents time series of the horizontal flux term for all of the above volumes. The figure only shows periods 4 (0000 GMT 13 November) to 13 (1200 GMT 17 November). Units are W m^{-2}.

However the positive contribution to $-\mathbf{V}_D \cdot \nabla\phi$ in volume 15C comes from the lowest layers with this term being strongly negative for periods 8 and 9 at jet level, while a major time contribution to the positive $-\mathbf{V}_D \cdot \nabla\phi$ term in the 15A volume comes from the jet level (~250 mb). This is illustrated by Fig. 21 which provides time series of the generation of kinetic energy by the divergent and rotational wind in the boundary layer (1000–900 mb) and at jet level (200–300 mb) for volumes 15A and 15C. As a consequence of this distribution the generation of KE in the cyclone environment is largely offset by friction in the boundary layer whereas downstream export is observed in the anticyclone volume. In this sense the region 15A acts as a much stronger net generator of KE than does the 15C volume for the time periods considered.

7. Discussion

A central feature of this discussion is the evolution of the anticyclone from a cold, polar high to a warm, dynamic system. Concurrently we also will consider the movement and structural changes of the cold air mass associated with this anticyclone. The complete description of these systems involves the synthesis of a number of concepts and quantities, such as potential vorticity, anticyclogenesis, jet streaks, and eddy available potential energy (EAPE), which are not often linked together in the literature.

An aspect of the anticyclone in its source region, Alaska, that should be clarified is the vertical extent of its circulation. The horizontal anticyclonic flow (negative relative vorticity) is for the most part restricted to a shallow layer below 850 mb but the vertical motions associated with the anticyclogenesis extend through the entire tropopause. Thus, in speaking of the shallow, polar anticyclone one must be careful not to extend the shallowness concept to all aspects of the system.

The anticyclone moves southward on the western flank of the associated cold dome. Since the anticyclone is not in the center of the coldest air (lowest 500–1000 mb thickness) this position on the thickness gradient sets up a pattern of geostrophic cold advection to the southeast of the anticyclone center (see Fig. 13 of Dallavalle and Bosart, 1975). The anticyclone tends to move southeastward toward this region of maximum descent forced by cold advection.

The cold dome as it moves southward is supported by a strong jet streak on its western side. This jet streak provides the shear necessary to maintain the thermal gradients as the cold air moves southward (Palmen and Newton, 1969). Concurrently the cold

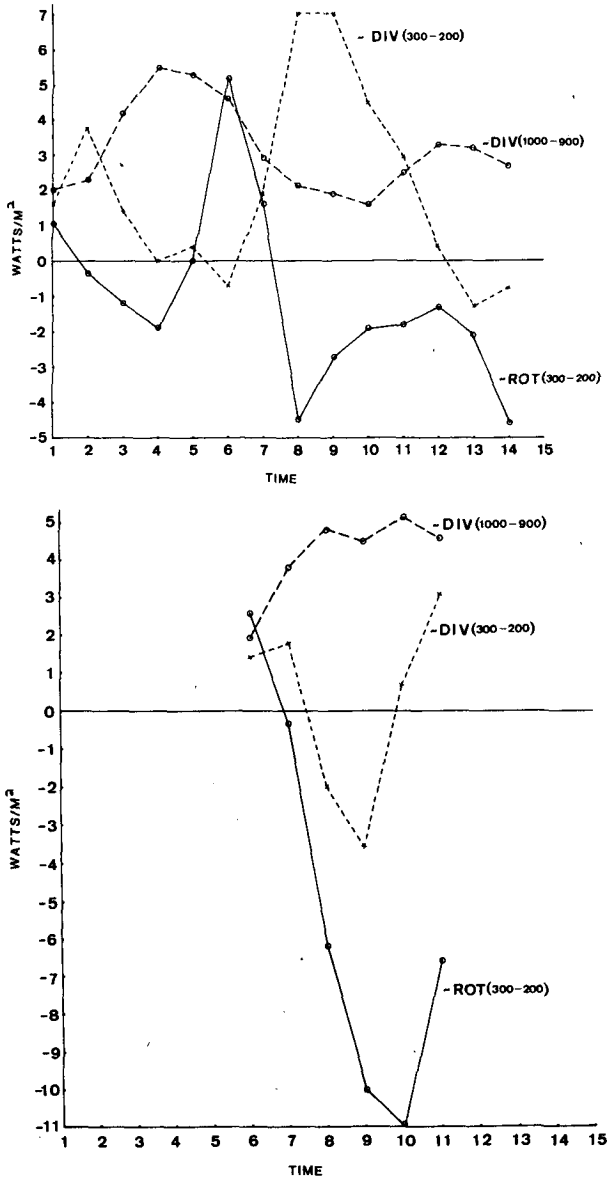

FIG. 21. Time series of the generation of kinetic energy by the rotational and divergent winds at jet level (300–200 mb) and by the divergent wind in the surface layer (1000–900 mb) for (A) the 15 × 15 anticyclone region and (B) the 15 × 15 cyclone region. Units are W m^{-2}.

dome is accompanied by a maximum of potential vorticity positioned aloft over the center of lowest thickness. The dynamic support provided by the potential vorticity maximum (Eliassen and Kleinschmidt, 1957) is an alternative and perhaps more complete way of viewing the processes of preserving the integrity of the cold dome represented by asymmetries of the jet streak.

Energetically one can see that both asymmetries in the jet stream and potential vorticity maxima explain how the atmosphere generates very large amounts of eddy available potential energy. Without such structures the cold dome could not move as far south but would subside and warm adiabatically once it leaves the source region.

After the anticyclone reaches the Gulf coast it begins to recurve northeastward along the Atlantic coast. Not only the direction of movement but also the nature of the forcing dictate movement changes at this time. Calculations show that the anticyclone as it moves northeastward is now tracking towards the descent maximum forced by differential vorticity advection. A sharp ridge has developed at upper levels to the west of the anticyclone to provide the negative vorticity advection over the Atlantic coast. This feature is also reflected in the strong cold advection in the lower stratosphere (100–300 mb thickness) directly over the future location of the anticyclone. Consistent with its altered structure the anticyclone (now warm) is directed by cold advection at upper levels, rather than at the lowest levels as it was previously.

Changes in the vertical structure of the anticyclone are also in accord with the evolution described in the preceding paragraph. The vertical spacing of the isentropes in Fig. 5 depicts how the static stability near the anticyclone center changes with time. The main feature to be noted is that the upper troposphere becomes less stable, while the lower troposphere (excluding the planetary boundary layer) becomes more stable. These changes in structure are consistent with the subsidence which is prevalent near the anticyclone center for all the time periods considered here. The changeover in static stability is concurrent with the changeover in the dominant forcing for the subsidence. The upper level forcing becomes more dominant as the stability is reduced aloft and increased below.

As the anticyclone proceeds to the northeast the cold dome begins its collapse. The sinking of the cold air is related to the fact that the upper level jet streak has now passed to the eastern side of the upper level trough. Thus the strong thermal gradients on the west side are no longer supported by the wind shear. This migration of the jet streak and the upper level frontal structure is a familiar feature of mid-latitude systems (Palmen and Newton, 1969). Related to this jet streak movement is the fact that the potential vorticity maximum begins to move to the northeast away from the center of the coldest air. This also indicates a decrease in the dynamic support of the cold dome. The displacement of the potential vorticity maximum towards warmer air has been shown to be a cyclogenetic process (Bleck, 1974). The development of the cyclone on the eastern flank of the cold dome is consistent both with the jet streak rounding the trough and the potential vorticity maximum shifting towards warmer air.

With respect to the energetics the movement of the potential vorticity maximum and jet streak allow a sinking of the cold air which represents a conversion from eddy available potential energy to kinetic en-

ergy. From the present work it is not clear how much of the energy released by the cold air collapse ($\omega'\alpha' < 0$) is converted into the kinetic energy of the storm, but the indication is that it is important to the development of the cyclone.

As the cyclone develops, the potential vorticity is not conserved near the storm center. Evidently diabatic processes lead to destruction of potential vorticity and tend to reduce the potential vorticity maximum to tropospheric values.

The quasi-Lagrangian energetics of the anticyclone and cyclone show that the anticyclone is not a wholly quiescent region. Indeed with respect to the general circulation it is shown that for this case the anticyclonic region provides considerably more net kinetic energy to the rest of the atmosphere than the cyclone for the time periods considered. The results indicate that the EAPE released by the cold dome collapse in the anticyclonic region provides an important energetic impetus to the cyclone by strengthening the upper level jet streak which is vital to the rapid development of the storm.

Acknowledgments. This work constitutes part of the Ph.D. thesis of the first author. We wish to thank Dr. Geoff Dimego for supplying the original objective analysis routines and Dr. Song C. Lin for his computational assistance. The authors are grateful to the reviewers for the valuable comments that led to improvement of the original manuscript. Ms. Marion Marks typed the manuscript and Ms. Kyong Lee assisted in drafting the figures. Support for this research was provided by National Science Foundation Grant ATM-802655702.

REFERENCES

Alpert, J. C., 1981: An analysis of the kinetic energy budget for two extratropical cyclones: The vertically averaged flow and the vertical shear flow. *Mon. Wea. Rev.*, **109**, 1219–1232.

Austin, J. M., 1947: An empirical study of certain rules for forecasting the movement and intensity of cyclones. *J. Meteor.*, **4**, 16–20.

Bleck, R., 1973: Numerical forecasting experiments based on the conservation of potential vorticity on isentropic surfaces. *J. Appl. Meteor.*, **12**, 737–752.

——, 1974: Short range prediction in isentropic coordinates with filtered and unfiltered numerical models. *Mon. Wea. Rev.*, **102**, 813–829.

——, 1975: An economical approach to the use of wind data in the optimum interpolation of geo- and Montgomery potential fields. *Mon. Wea. Rev.*, **103**, 807–816.

——, and P. L. Haagenson, 1968: Objective analysis on isentropic surfaces. NCAR Tech. Note TN-39, 27 pp.

Bodurtha, F. T., 1952: An investigation of anticyclogenesis in Alaska. *J. Meteor.*, **9**, 118–125.

Boyle, J. S., 1981: Autocorrelations of moisture parameters on isentropic surfaces. *Mon. Wea. Rev.*, **109**, 2401–2404.

Chen, T. C., and L. F. Bosart, 1977: Quasi-Lagrangian kinetic energy budgets of composite cyclone-anticyclone couplets. *J. Atmos. Sci.*, **34**, 452–464.

Dallavalle, J. P. and L. F. Bosart, 1975: A synoptic investigation of anticyclones accompanying North American polar air outbreaks. *Mon. Wea. Rev.*, **103**, 941–957.

Danard, M. B., 1964: On the influence of released latent heat on cyclone development. *J. Appl. Meteor.*, **3**, 27–37.

——, and G. E. Ellenton, 1980: Physical influences on east coast cyclogenesis. *Atmos. Ocean*, **18**, 65–82.

Danielsen, E. F., 1968: Stratospheric-tropospheric exchange based on radioactivity, ozone, and potential vorticity. *J. Atmos. Sci.*, **25**, 502–518.

——, and S. Hipskind, 1980: Stratospheric-tropospheric exchange at polar latitudes in summer. *J. Geophys. Res.*, **85**, 393–400.

Eliassen, A., and E. Kleinschmidt, Jr., 1957: Dynamic meteorology. *Handbuck der Physik*, Vol. 48, Springer-Verlag, 1–154.

Endlich, R. M., 1967: An iterative method for altering the kinematic properties of wind fields. *J. Appl. Meteor.*, **6**, 837–844.

Fleagle, R. G., 1947: The fields of temperature, pressure, and three-dimensional motion in selected weather situations. *J. Meteor.*, **4**, 165–185.

Gall, R. L., and D. R. Johnson, 1977: A comparison of two methods for estimating sensible heat flux in oceanic extratropical synoptic scale systems. *Tellus*, **29**, 222–228.

Holopainen, E., 1973: An attempt to determine the effects of turbulent friction in the upper troposphere from the balance requirements of the large scale flow: A frustrating experiment. *Geophysica*, **12**, 151–176.

Holton, J. R., 1979: *An Introduction to Dynamic Meteorology.* Academic Press, 319 pp.

Hoskins, B. J., I. D. Draghici and H. C. Davies, 1978: A new look at the omega equation. *Quart. J. Roy. Meteor. Soc.*, **104**, 31–38.

——, and M. A. Pedder, 1980: The diagnosis of middle latitude synoptic development. *Quart. J. Roy. Meteor. Soc.*, **106**, 707–719.

Kondo, J., 1975: Air-sea bulk transfer coefficients in diabatic conditions. *Bound. Layer Meteor.*, **9**, 91–112.

Krishnamurti, T. N., 1968: A diagnostic balance model for studies of weather systems of low and high latitudes: Rossby number less than 1. *Mon. Wea. Rev.*, **96**, 197–207.

Kung, E. C., and W. E. Baker, 1975: Energy transformations in middle latitude disturbances. *Quart. J. Roy. Meteor. Soc.*, **101**, 793–815.

O'Brien, J. J., 1970: Alternative solutions to the classical vertical velocity problem. *J. Appl. Meteor.*, **9**, 197–203.

Palmèn, E., and C. W. Newton, 1969: *Atmospheric Circulation Systems.* Academic Press, 603 pp.

Pearce, R. P., 1974: The design and interpretation of diagnostic studies of synoptic-scale atmospheric systems. *Quart. J. Roy. Meteor. Soc.*, **100**, 265–285.

Petterssen, S., 1956: *Weather Analysis and Forecasting.* 2nd ed. McGraw Hill, 428 pp.

——, D. L. Bradbury and K. Pedersen, 1962: The Norwegian cyclone models in relation to heat and cold sources. *Geofys. Publ.*, No. 24, 243–280.

Reiter, E., 1969: *World Survey of Climatology*, Vol. 7. Elsevier Scientific, 443 pp.

Schlatter, J. T., G. W. Branstator and L. G. Thiel, 1976: Testing a global multivariate statistical objective analysis scheme with observed data. *Mon. Wea. Rev.*, **104**, 765–783.

Smith, P. J., 1973: Mid-latitude synoptic scale systems: their kinetic energy budgets and role in the general circulation. *Mon. Wea. Rev.*, **101**, 757–762.

Staley, D. O., 1960: Evaluation of potential-vorticity changes near the tropopause and the related vertical motions, vertical advection of vorticity, and transfer of radioactive debris from stratosphere to troposphere. *J. Meteor.*, **17**, 591–620.

Trenberth, K. E., 1978: On the interpretation of the diagnostic quasi-geostrophic omega equation. *Mon. Wea. Rev.*, **106**, 131–137.

Uccellini, L. W., and D. R. Johnson, 1979: The couplings of upper and lower tropospheric jet streaks and implications for the development of severe convective storms. *Mon. Wea. Rev.*, **107**, 682–703.

Vincent, D. G., and L. N. Chang, 1973: Some further considerations concerning energy budgets of moving systems. *Tellus*, **25**, 224–232.